Ocean Dynamics (2014) 64:557–571
DOI 10.1007/s10236-014-0703-z

On the dynamics of low latitude, wide and shallow coastal system: numerical simulations of the Upper Gulf of Thailand

Suriyan Saramul · Tal Ezer

Received: 9 August 2013 / Accepted: 29 January 2014 / Published online: 25 February 2014

Abstract A high-resolution (~1 km horizontal grid and 21 vertical layers) numerical model based on the Princeton Ocean Model (POM) has been used to study the 3D dynamics of the Upper Gulf of Thailand (UGOT). While influenced by tides and rivers like other estuarine systems, the UGOT is unique because it is wide (~100 km×100 km), it is shallow (average depth of only ~15 m), it is located in low latitudes (~12.5°N–13.5°N), and it is influenced by the seasonal monsoon. Sensitivity studies were thus conducted to evaluate the impact that surface heat fluxes, monsoonal winds, river runoffs, and the low latitude may have on the dynamics; the latter has been evaluated by modifying the Coriolis parameter and comparing simulations representing low and mid latitudes. The circulation in the UGOT changes seasonally from counter-clockwise during the northeast monsoon (dry season) to clockwise during the southwest monsoon (wet season). River discharges generate coastal jets, whereas river plumes tend to be more symmetric near the river mouth and remain closer to the coast in low latitudes, compared with mid-latitude simulations. River plumes are also dispersed along the coast in different directions during different stages of the monsoonal winds. The model results are compared favorably with a simple wind-driven analytical estuarine model. Comparisons between an El Niño year (1998) and a La Niña year (2000) suggest that water temperatures, warmer by as much as 2 °C in 1998 relative to 2000, are largely driven by decrease cloudiness during the El Niño year. The developed model of the UGOT could be used in the future to address various environmental problems affecting the region.

Keywords Numerical model · Monsoon · Tides · Rivers · Upper Gulf of Thailand

Responsible Editor: Jarle Berntsen

This article is part of the Topical Collection on the *5th International Workshop on Modelling the Ocean (IWMO) in Bergen, Norway 17-20 June 2013*

S. Saramul
Department of Marine Science, Chulalongkorn University, Phyathai Road, Pathumwan, Bangkok 10330, Thailand

T. Ezer (✉)
Center for Coastal Physical Oceanography, Old Dominion University, 4111 Monarch Way, Norfolk, VA 23508, USA
e-mail: tezer@odu.edu

1 Introduction

The dynamics of semi-enclosed basins and coastal regions are often fall into one of two categories, either a dominantly wind-driven system, or an estuarine-like system driven by tides and river discharges. The motivation for this study of the Upper Gulf of Thailand (UGOT) comes from the fact that this area is unique in its topography and location and thus its dynamics may involve characteristics of both a shallow wind-driven system associated with the seasonal monsoonal winds and an estuarine-like system associated with tides and buoyancy-driven river flows. This region is especially vulnerable to impacts of climate change, since seasonal monsoonal floods may become more severe due to fast sea level rise (SLR) in this region. In some locations in the northern UGOT, the relative SLR can be as much as ten times faster than the global mean SLR (Saramul 2013). Land subsidence on Thailand's coasts is especially large due to earthquakes and groundwater extractions (Nicholls 2011), which results in large spatial variations in relative SLR that significantly exceed those at other places with land subsidence (e.g., the U.S. East coast; Ezer 2013). Other environmental problems, such as pollutants carried by rivers and coastal erosion, will require a better knowledge of the circulation and forcing mechanisms in the UGOT. In a region with limited oceanic observations, these problems can be addressed with the help of a 3D numerical

coastal ocean model as done here. This UGOT area has not been modeled or studied as much as many other semi-enclosed seas at higher latitude such as the North Sea (e.g., Albretsen and Røed 2010).

In coastal systems that are long and narrow, steady wind-induced circulation can often be described with relatively simple barotropic models (Winant 2004; Sanay and Valle-levinson 2005), whereas only bottom topography and wind are considered (the Coriolis parameter, f, can be neglected if the basin or estuary is narrow enough relative to the Rossby Radius of deformation). In such cases, the dynamics is generally described by alongshore wind-induced transport in the direction of the wind in shallow areas and transports against the wind direction in deeper regions. For example, Csanady (1973) used an analytical model of Lake Ontario (a long and narrow lake) to show a flow pattern similar to the type described above. However, in a rotating system, or when stratification is not neglected, the transport pattern can be more complex. A simple model, like those mentioned above, will be compared here with a more realistic 3D baroclinic numerical model to evaluate the extent of which the basic wind-driven shallow dynamics can describe the circulation in the UGOT. On the other hand, in estuarine-like coastal systems, river flow and tidal mixing play the dominant roles, but wind is sometimes neglected. River plumes of freshwater create buoyancy flows and can contribute to the dynamic of the coastal circulation (Horner-Devine 2009). Due to the Coriolis effect, river plumes are deflected to the right/left in the Northern/Southern hemisphere and the coastal current will generally carry the plume away from the river mouth (Horner-Devine 2009). This dynamics assumes that there is a relatively large river discharge and that the Coriolis term is large enough (i.e., non-equatorial regions). Therefore, another purpose of the study is to evaluate the dynamics of river plumes in low latitudes, and hence, better understand how properties such as pollutants, salinity, and temperature in the coastal region are affected by the advection and mixing of river plumes in the UGOT.

The UGOT is a shallow (average depth of ~15 m), semi-enclosed basin, with almost a square (~1°×1°) shape; it is situated in low latitudes (~12.5°N–13.5°N), at the head of the Gulf of Thailand, which is also relatively shallow compared to the South China Sea nearby (Fig. 1). It is located in a region that is strongly affected by monsoonal winds and where four major rivers discharge (Fig. 2). A satellite image taken during a flood in 2011 shows a very axisymmetric river plume (Fig. 2a), with no apparent deflection to the right of the river flow (i.e., westward), as expected in the northern hemisphere; numerical model simulations will be used to test if this observation is the result of the low latitude of the UGOT.

The seasonal monsoon pattern includes a wet season when winds prevail from the southwest direction, a dry season when winds prevail from the northeast direction, and transitional periods in between (Fig. 3e). Previous numerical model studies suggest that the southwest/northeast monsoonal winds drive clockwise/counter-clockwise circulation in the UGOT (Buranapratheprat et al. 2008b, 2009). However, the previous studies used only monthly mean winds, while here more realistic semi-daily wind forcing, as well as daily heat fluxes will be used (Fig. 3).

Multi-year simulations will allow us to look at interannual variations, and test the influence of large-scale climate variations associated with El Niño and La Niña. In particular, the El Nino-Southern Oscillation (ENSO) has large influence on precipitation and cloudiness over the region (Chandra et al. 1998), which could affect air-sea heat exchange and water temperatures. Studies show the influence of ENSO on the circulation in the South China Sea (Chao et al. 1996), so it is likely that ENSO influences the UGOT as well. Unlike mid- and high- latitudes, surface heat fluxes in the UGOT (Fig. 3a, b) do not show significant seasonal cycles that can explain the seasonal variations in surface temperature (Fig. 3c). However, large seasonal variations are seen in cloud coverage (Fig. 3d) and winds (Fig. 3e), as a result of the seasonal monsoon cycle. The southwest monsoonal winds (about days 90–300) bring warm and moist air from the southwest and the sky is largely covered with clouds. Note that in 1997–1998 there was an El Niño event, with warmer temperatures and longer period of clear sky, while in 1999–2000 there was a La Niña event, with colder temperatures and more cloud cover. Therefore, the influence of ENSO will be addressed in this study.

The study follows previous 3D estuarine circulation modeling of the impact of winds, tides, and freshwater discharges in places such as the Chesapeake Bay (Guo and Valle-Levinson 2007, 2008), the Charlotte Harbor estuary (Zheng and Weisberg 2004) and even in the UGOT (Buranapratheprat et al. 2008b, 2009), but will focus on studying the particular characteristics of the UGOT, including its topography, forcing mechanisms, and location in low latitudes.

The paper is organized as follows: in Section 2, the numerical model and the experiments are described; in Section 3, the seasonal wind- and river-driven circulations are described; in Section 4, the numerical model is compared with a simple analytical model; in Section 5, interannual variations and ENSO impact are described; and finally, Section 6 offers discussions and conclusions.

2 Model description, forcing data, and experimental design

The model used in this study is based on the Princeton Ocean Model (POM; Blumberg and Mellor 1987; Mellor 2004). The POM is a 3D, free surface, primitive equation ocean model that includes a complete thermodynamics and the level 2.5 Mellor–Yamada turbulence closure scheme (Mellor and Yamada 1982) to provide vertical mixing. Bottom friction is

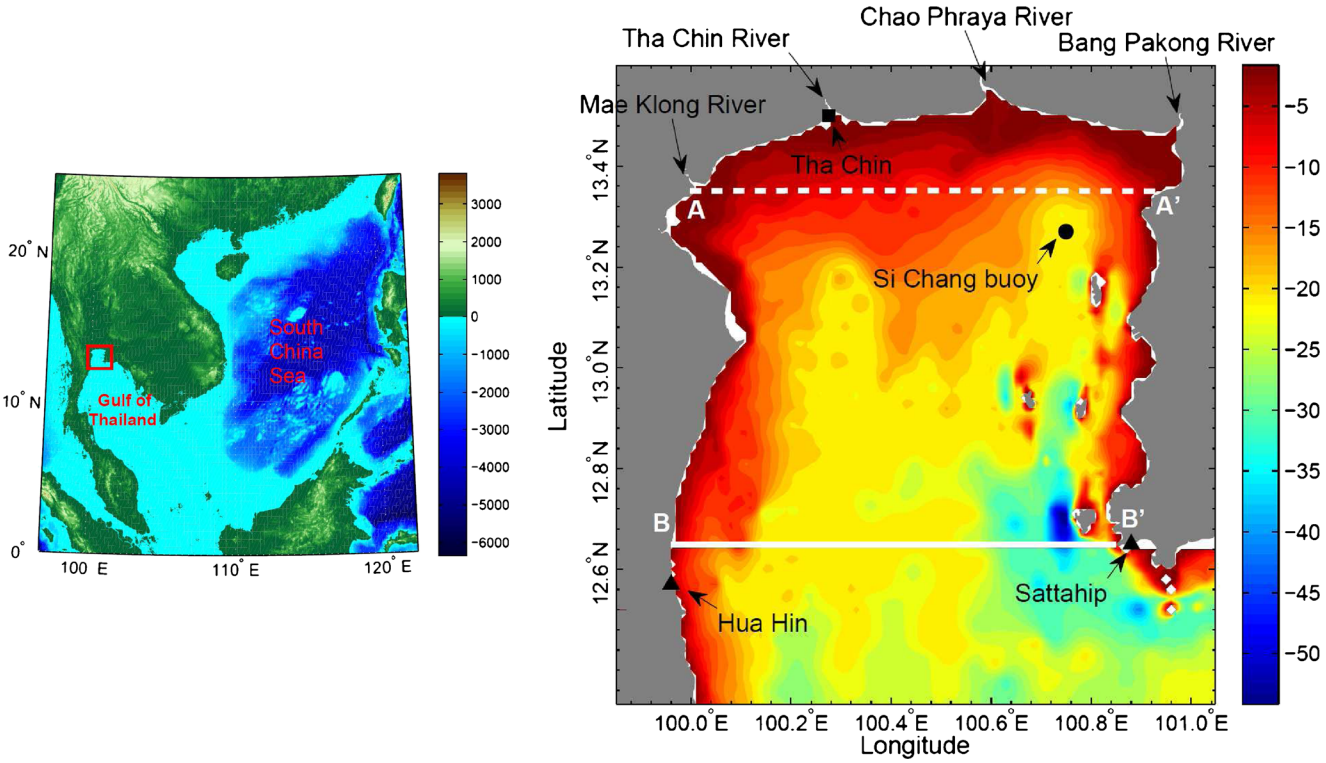

Fig. 1 *Left* The topography of the region, including the South China Sea and the Gulf of Thailand; the study area is indicated by the *red box*. *Right* Focus on the topography of the study area in the Upper Gulf of Thailand. *Color* represents bottom depth in m. The southern boundary of the numerical model is the B-B′ solid line where astronomical tides were imposed, using the sea level data from the two tidal stations near B and B'. Dashed line A-A′ is the cross-section shown in Fig. 6. The locations of four major rivers at the head of the model domain are indicated, as well as the tide gauge station (*black square*) and the buoy station (*black circle*) used to evaluate the model in Fig. 4

based on "law of the wall" formulation for boundary layers (see Mellor 2004) with maximum drag coefficient of 0.0025. The model domain and bottom topography of the UGOT are shown in Fig. 1. The average depth of the UGOT is only 15 m, which includes a smooth bottom in most of the domain, except some deeper channels and more complex topography around islands along the eastern boundary. The horizontal grid is curvilinear, but is almost rectangular with grid cells $\Delta x \sim \Delta y \sim 1$ km. In the vertical direction, z, a terrain-following, sigma-coordinate grid, σ, is used with n=21 layers, i.e., $\sigma_i = (z_i - \eta)/(H + \eta)$; whereas $-1 < \sigma_i < 0$ and $-H < z_i < \eta$, for $i = 1,\ldots,n$, where $H(x,y)$ and $\eta(x,y,t)$ are the bottom depth and surface elevation, respectively. The minimum depth in the model is set to 3 m, which is sufficient for simulations of tides in the UGOT without inundation. Simulations with the wetting and drying option in POM (e.g., Saramul and Ezer 2010), which could simulate much shallower regions of few centimeters deep, will be considered in future studies.

At the southern open boundary (B-B′ line in Fig. 1), a radiation boundary condition is applied to allow waves to propagate across the boundary without reflection (Mellor 2004). The open boundary conditions for temperature and salinity allow properties set on the boundary from observations (see below) to be advected into the model domain when flow is northward. Tidal forcing includes 8 tidal constituents, Q1, O1, P1, K1, N2, M2, S2, and K2, obtained from harmonic analysis of observed surface elevations at 2 tide gauge stations located near the two edges of the southern boundary (Fig. 1). Linear interpolated between these 2 stations is used and applied to the boundary as a combination of tidal elevation and barotropic flow boundary conditions (Mellor 2004). Initial conditions of salinity and temperature are based on observations (Buranapratheprat et al. 2008a). Salinity is initially assigned as a constant (32.15; dimensionless units of Practical Salinity Scale, PSS) for the entire model domain, while water temperature is nearly constant and it is varied from 30.63 °C at the surface to 30.02 °C at the bottom, based on typical observed profiles. After spin-up (which is very short, order of weeks for such a shallow basin) the model ran for the period 1997–2000. All the sensitivity experiments discussed in Section 3 are based on simulations with different forcing fields and different parameters representing the year 2000, and only in Section 5 interannual variations are discussed.

Surface forcing fields are shown in Fig. 3. These data are daily and spatially uniform. Reliable data with high resolution spatial distributions are not available for this region. However, since this study aims to understand processes with sensitivity experiments using different forcing and is not aimed at developing a realistic ocean forecast system, the assumption of

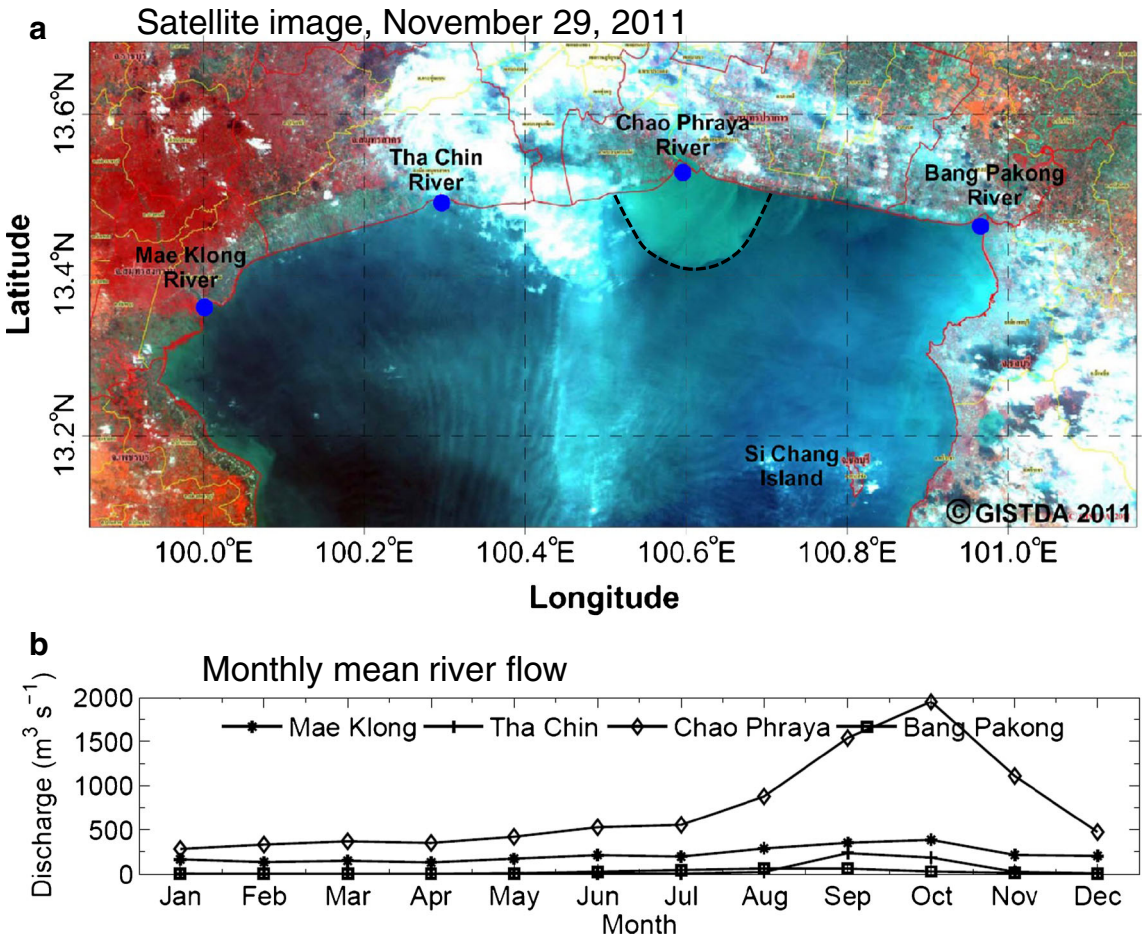

Fig. 2 **a** A false color image from the THEOS satellite taken in November 29, 2011, during a major flood. The edge of a turbidity plume from the Chao Phraya River is indicated by the *dashed black line*. *White* and *red areas* are clouds and land vegetations, respectively. This image is modified (with permission) from the original image obtained from www.gistda.or.th/gistda_n/Gallery/img/Flood2011. **b** Monthly mean river discharges of the four major rivers shown in **a** and used by the model

uniform forcing fields seems justified. Note, however, that despite the spatial uniform surface forcing, the model developed quite realistic spatial patterns of surface temperatures due to the ocean dynamics. Surface wind stress for the sensitivity experiments during 2000 is based on the 10-m wind vectors retrieved semi-daily from Jet Propulsion Laboratory (poet.jpl.nasa.gov); for the interannual simulations (1997–2000) daily fields are obtained from the European Center for Medium range Weather Forecasting (ECMWF) reanalysis data (data-portal.ecmwf.int/data/d/era40_daily). Surface heat fluxes in the model are implemented based on the approach described in Ezer (2000) with some modification needed for this region. The heat fluxes, Q, in the model is calculated by

$$Q = Q_o + \left(\frac{\partial Q}{\partial T}\right)(T_o - T_m) + Q_{sw} \times F_s \qquad (1)$$

where Q_o is the observed net flux (Q_{net}) without shortwave radiation (Q_{sw}). The second term is a feedback term, where T_o and T_m are surface temperature obtained from observed and model data, respectively, and the coupling coefficient, $\partial Q/\partial T$, is set to 50 W m^{-2} K^{-1} (Ezer 2000). The third term is shortwave radiation, which allows solar radiation to penetrate into the upper few meters of the ocean (Mellor 2004). In this region, with large seasonal variations in cloud cover (Fig. 3d) due to the dry/wet monsoon periods, it became apparent that cloud cover must be taken into account as it strongly affect the amount of short wave radiation reaching the surface of the water. F_s is the clear sky factor calculated as 0.6+0.4×(% Clear sky/100), based on trial and error tests. The clear sky factor is estimated from satellite-derived sea surface temperature retrieved from AVHRR Pathfinder version 5 (http://poet.jpl.nasa.gov). Q_{net}, Q_{sw}, and T_o are obtained from reanalyzed data from the work of Yu et al. (2008), and retrieved from http://rda.ucar.edu.

The implementation of rivers in the model is based on the work of Oey (1996), whereas river discharge Q_{riv} is considered as freshwater vertical flux upstream the river mouth. The monthly water discharges in four rivers are shown in Fig. 2b. Maximum river flow is in September–

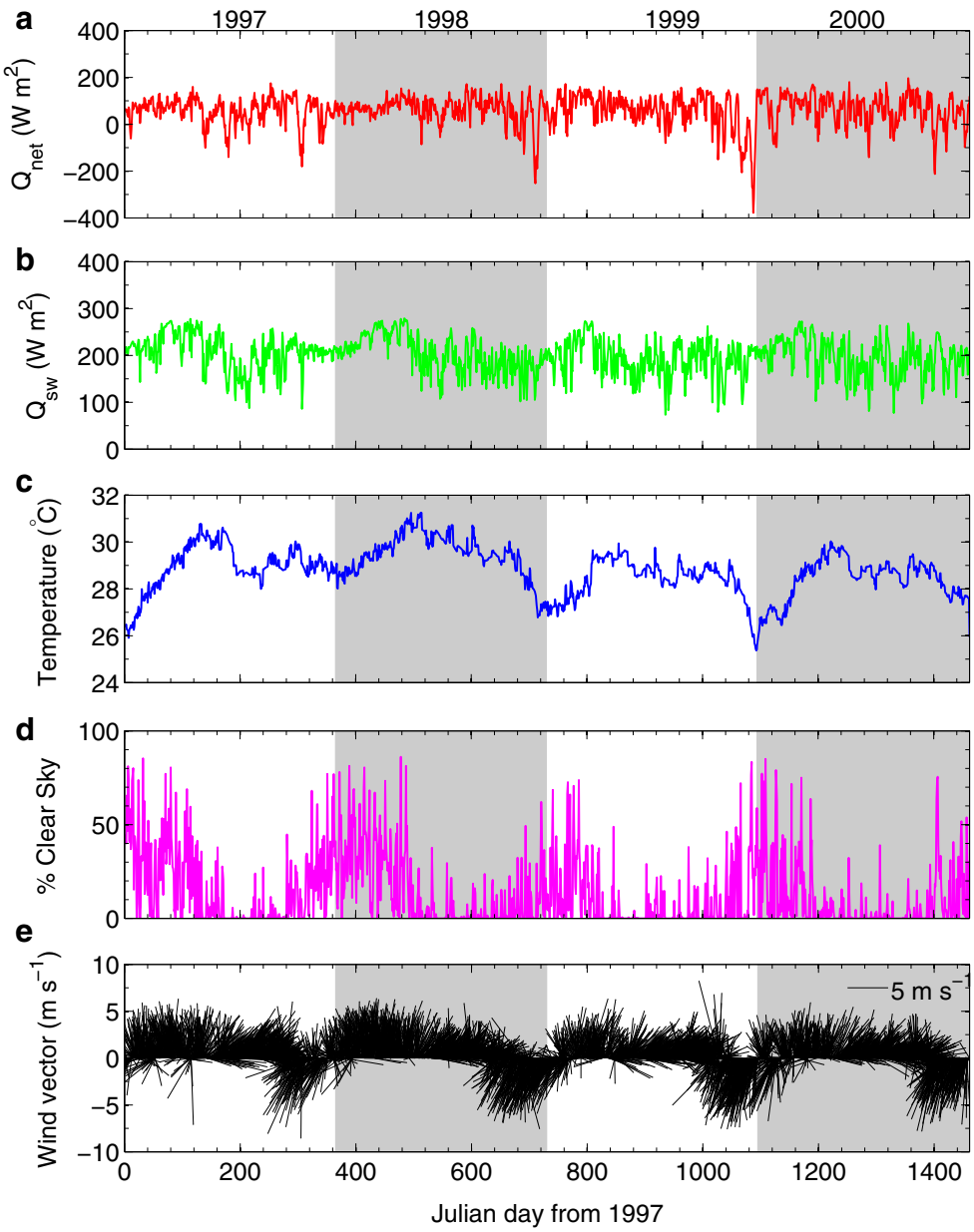

Fig. 3 Surface forcing data used in the model (Eq. 1): **a** net heat fluxes, Q_{net}; **b** shortwave radiation, Q_{sw}; **c** surface temperature, T_o; **d** % clear sky; and **e** wind vectors

October, during the transition from the southwest to northeast monsoons. Note that interannual variations in river flows are neglected here.

Table 1 summarizes the six experiments analyzed here to investigate the separate impact of winds (experiments Wnd_1 and Wnd_2), river discharges (Riv_1 and Riv_2), and the combined impact of winds and rivers (WRiv_1 and WRiv_2). The impact of the Coriolis parameter, f, is evaluated by comparing experiments denoted exp_1 (real UGOT location in low latitude) and exp_2 (mid-latitudes). The Coriolis parameter in the model varies in space (function of latitude), but its spatial variation in each experiment is not significant in such a small domain. Surface salinity, surface temperature, and current velocity obtained from the model results are saved hourly and the monthly averaged values of these parameters are discussed in the following sections.

Table 1 Model experiments

Experiment	Forcing	Model domain center
Wnd_1	Surface heat fluxes, tides, wind	~13°N
Wnd_2	Surface heat fluxes, tides, wind	~45°N
Riv_1	Surface heat fluxes, tides, rivers	~13°N
Riv_2	Surface heat fluxes, tides, rivers	~45°N
WRiv_1	Surface heat fluxes, tides, wind, rivers	~13°N
WRiv_2	Surface heat fluxes, tides, wind, rivers	~45°N

Because of the importance of tidal mixing, all the experiments in Table 1 include tides. The performance of the tidal model is evaluated against observations and examples of model-data comparisons for surface elevation and currents are shown in Fig. 4. Tidal velocity in the UGOT is mainly in the north–south direction, so only *v*-velocity is shown. Both surface elevation and *v*-velocity obtained from the tidal model are compared well with observed data; the Root Mean Square Error is 16.9 cm for elevation and 3.75 cm s^{-1} for velocity, and the data-model correlation coefficients are larger than 0.9 for both fields. More detailed analysis of model and observed tides, as well as sea level data, can be found in Saramul (2013).

3 Model results

3.1 Seasonal wind-driven circulation and dynamics

First, simulations of the seasonal wind-driven sub-tidal circulation based on experiment Wnd_1 (i.e., wind forcing, but no rivers) are described. Examples of monthly mean surface elevations anomaly and depth-averaged velocities are shown in Fig. 5, representing four seasons, first inter-monsoon (March), southwest monsoon (May), second inter-monsoon (October), and northeast monsoon (November). The most apparent pattern is that during the southwest monsoon (May–September), the prevailed winds cause the water in the UGOT to pileup on the northeast corner of the domain and the circulation is mostly clockwise (Fig. 5b), while during the northeast monsoon (November–February), a counter-clockwise circulation is developed, with lower water level in the northeast (Fig. 5d). During the first and second inter-monsoons the surface elevation has a north–south (Fig. 5a) and east–west (Fig. 5c) patterns, respectively. While the flow along the northern and western coastal boundaries are relatively smooth, the larger variations in bottom topography and the existence of islands along the eastern boundary (Fig. 1) result in more complex circulation patterns and the developments of small (~10–20 km in size) gyres (e.g., at 100.8°E, 13.3°N, there is a gyre with an anti-clockwise circulation in March and a clockwise circulation in November). Note that the circulation is far from a geostrophic balance since the flow is mostly across lines of constant elevation and not parallel to them (e.g., in Fig. 5c, the flow along the northern coast is eastward, while the surface elevation contours are in the north–south direction). The flow seems to resemble non-rotating wind-driven circulation in shallow basins (Csanady 1973; Sanay and Valle-levinson 2005), whereas the flow tends to be in the direction of the wind along the shallow areas near the coast.

To evaluate the 3D vertical distribution of the wind-driven flow, the velocity distribution along an east–west cross section (line A-A′ along 13.35°N in Fig. 1) is shown in Fig. 6 for the same months as those shown for the horizontal circulation in Fig. 5. Large seasonal variations in the vertical structure are noticeable, with periods of more barotropic flow and periods of more baroclinic flow (i.e., depth-dependent). During the

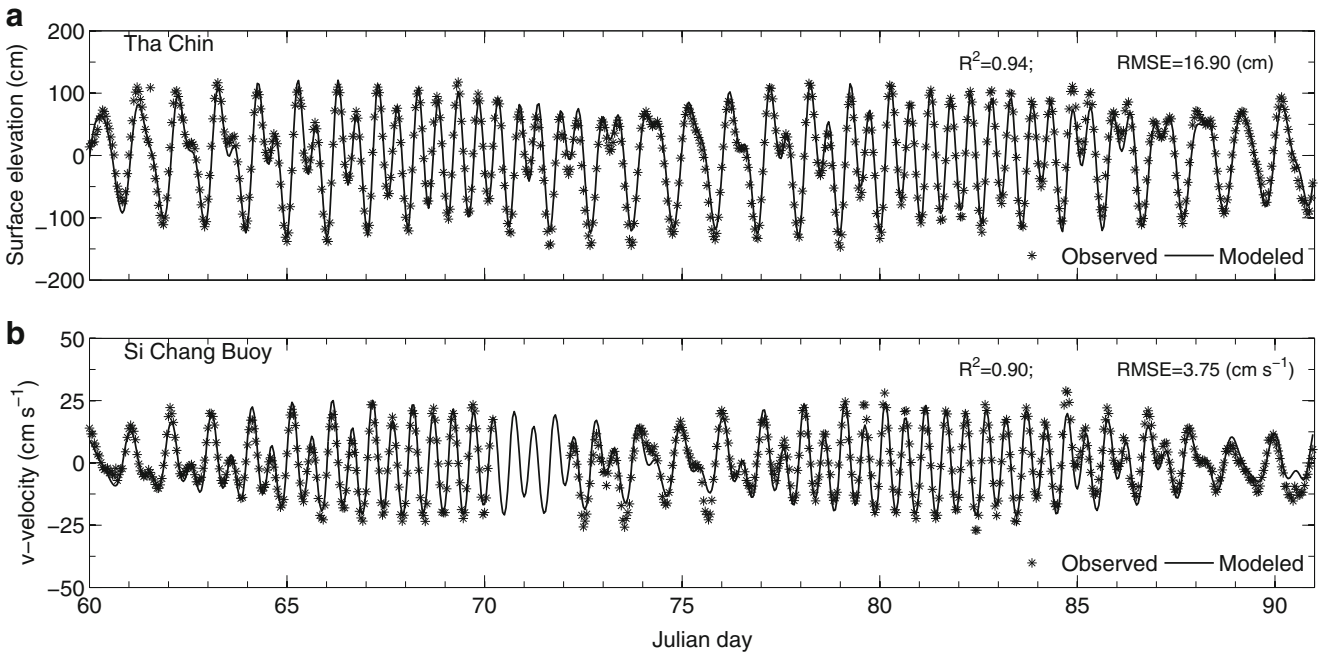

Fig. 4 Examples of model-data comparisons during March 2000 for **a** surface elevation at Tha Chin tide gauge station and **b** *v*-velocity at Si Chang buoy station (see Fig. 1 for locations). Observed points are marked with *stars*, and model output with *solid lines*. Correlation coefficients between the data and the model, R^2, and root mean squared errors (RMSE) are depicted on the *top right corner of each panel*

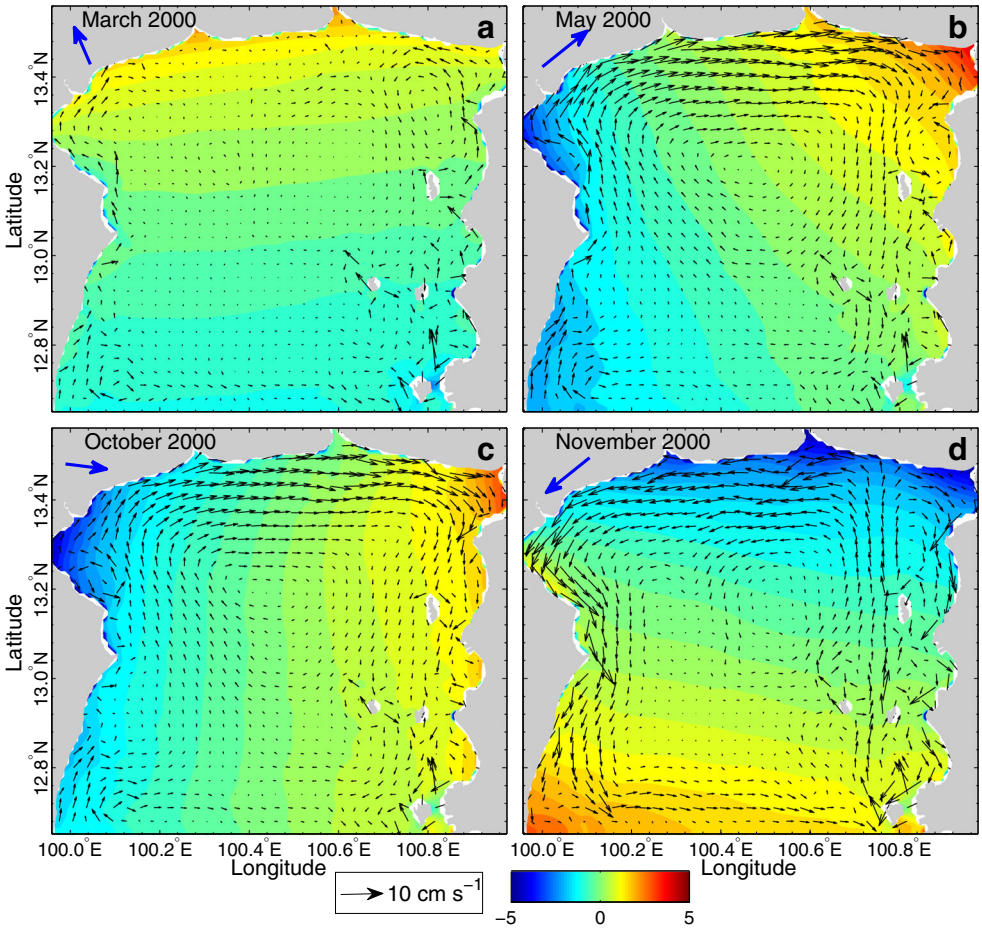

Fig. 5 Monthly mean and depth-averaged current velocity (*black arrows*, in cm s^{-1}) and monthly mean surface elevation anomaly (*color*, in cm) obtained from experiment Wnd_1 for four different monsoon seasons during 2000: **a** first inter-monsoon (March), **b** southwest monsoon (May), **c** second inter-monsoon (October), and **d** northeast monsoon (November). Surface elevation anomaly is relative to the area averaged value of each month. *Blue arrows at the top left of each panel* show the mean monthly wind; for scaling reference, the wind speed in May is ~5 m s^{-1}

southerly wind (March), the *u*-velocity (along the section) is almost uniformly eastward throughout the entire water column (Fig. 6a), while the *v*-velocity (across the section) is a 2-layer flow with northward flow in the upper ~5–10 m and southward flow in the deep layer. The eastward *u*-velocity flow intensified near the surface in May and October (Fig. 6c, e), reflecting the coastal jet shown in Fig. 5, but the flow is completely reversed in November (Fig. 6g) during the northeastern monsoon. Note that in the deeper channel (around 100.7°E), there is a convergence in March, May, and October, but divergence in November (Fig. 6g). During November, the across-section flow (*v*-component) shows a southward upper layer flow, in the direction of the wind, and a northward subsurface jet of return flow in the center of the channel (Fig. 6h). More details of the November circulation will be discussed later with the help of an analytical model.

The vertical structure of flows may depend on three parameters (Kasai et al. 2000; Valle-Levinson et al. 2003): the vertical mixing coefficient, K_M, (derived in the model from the Mellor-Yamada turbulence scheme), the Ekman number $E_k = K_M/f H_0^2$ (which represents the importance of viscosity versus geostrophy; H_o is a depth scale, taken here as the maximum bottom depth), and the Ekman layer depth $D_E = \sqrt{2K_M/f} = \sqrt{2E_k}H_0$ (which represents the influence of the wind). Estimation of the average value of these parameters across the section in Fig. 6 is shown in Table 2. The Ekman number thus is proportional to the ratio between the Ekman layer depth and bottom depth, showing what portion of the water column is affected by wind-driven Ekman transport. For large Ekman number (i.e., small *f* or large K_M), $E_k=1$ and *f* can be neglected (Kasai et al. 2000), which leads to $D_E=1.4H_0$. Therefore, in such a case, the Ekman layer can occupy the entire water column and the pattern of flow across will be in a form of an inflow in one direction in the deeper part and return flow in opposite direction on the shoals (Wong 1994). If on the other hand, the Ekman number is moderately small, say $E_k=0.1$, then $D_E=0.45H_0$. This means that the upper part of the water column is controlled by *f*, while the lower half may be affected by a separate Ekman bottom layer. In the case of very small Ekman number, say $E_k=0.01$ or $D_E=0.14H_0$, the vertical eddy viscosity is weak, the flow is nearly geostrophic and the Ekman layer is pressed near the bottom (i.e., a two-layer flow is expected). In the simulations shown in Fig. 6, the Ekman number range (Table 2) is between 0.3 (March) and 1.2 (October), thus the flow is clearly not geostrophic. October is the only month with $E_k>1$, and thus, the along-channel flow

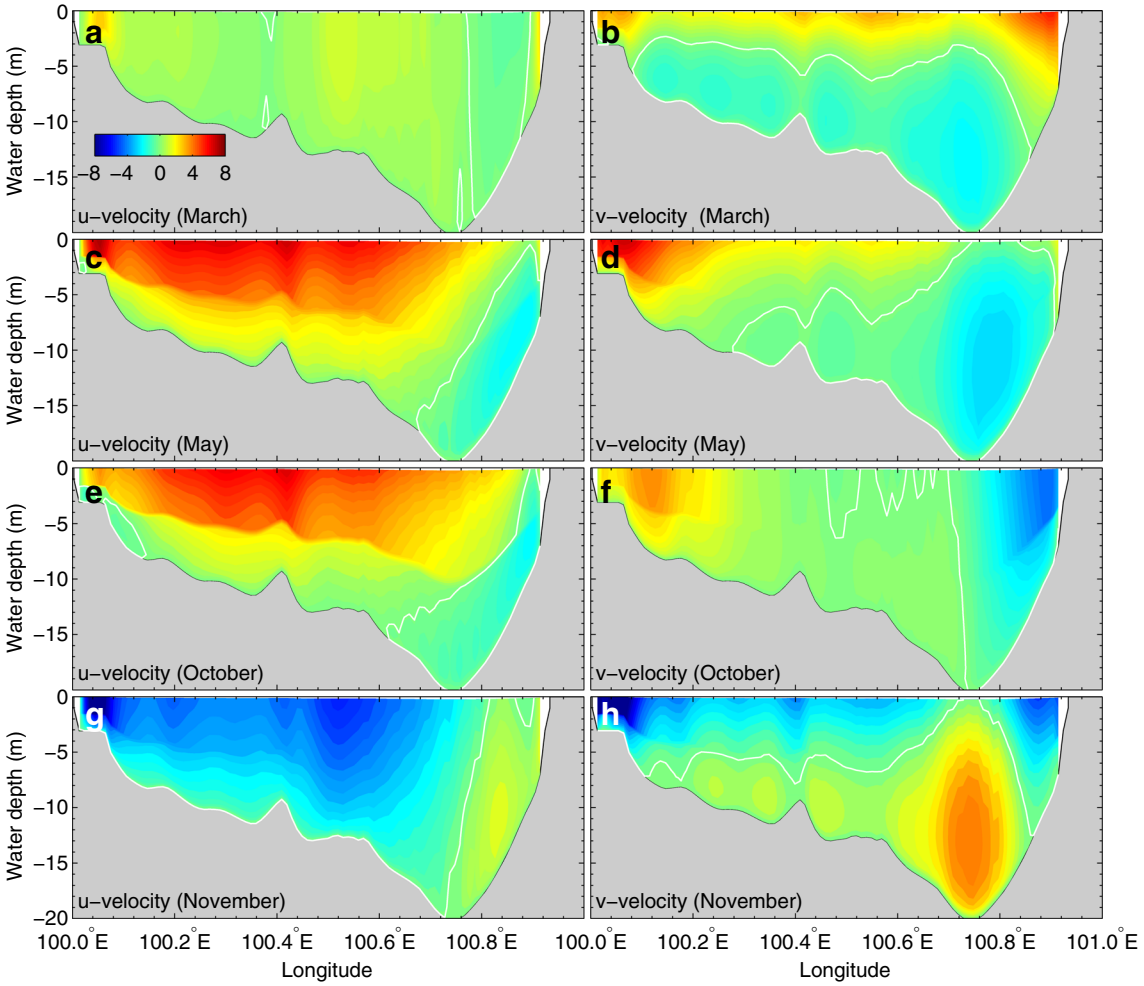

Fig. 6 Cross section of monthly mean (same months as Fig. 5) velocity distribution (in cm s^{-1}) of along-section, *u*-velocity (*left panels*) and across-section, *v*-velocity (*right panels*) along latitude 13.35°N (line A-A′ in Fig. 1). *White solid lines* separate between positive and negative velocities

is quite barotropic (Fig. 6f) with southward flow on the eastern side of the channel throughout the water column and northward westward of the deepest point. During the other months, a two-layer system is developed (with Ekman layer occupying only portion of the water column) as expected in cases of moderately small Ekman number. Note that the vertical structure depends on the Coriolis parameter, *f*, which is small, but not totally negligible, in the low latitudes of the UGOT; in the next section, the impact of Coriolis will be further evaluated.

Table 2 Vertical eddy viscosity (K_M), Ekman number (E_k), and Ekman depth (D_E) spatially averaged along latitude 13.35°N (line A-A′ in Fig. 1) and monthly averaged for March, May, October, and November 2000 (experiment Wnd_1)

Month	K_M (m^2 s^{-1})	E_k	D_E (m)
March	0.0033	0.3	14.2
May	0.0077	0.6	21.8
October	0.0164	1.2	31.7
November	0.0065	0.5	20.0

Figure 7 summarizes the seasonal north/south transport across the section shown in Fig. 6. During the period of southerly or southwesterly wind (March and May), a northward transport occupies the shallow regions in the west while a southward transport exists in the deeper channel in the east. During the northeasterly wind, the flow pattern reverses, so the southward and northward transports are located at the shallow and deeper regions, respectively. November seems to have especially large transport, centered at the deeper channel, because the wind is strongest. Even though bottom friction and Coriolis effects are included in the numerical experiment Wnd_1, the results seem to agree to some degree with the analytical results for the non-rotating frictionless coastal system shown in Csanady (1973).

3.2 River plume dynamics and the impact of Coriolis

To evaluate the impact of winds and Coriolis on the dynamics of river plumes, experiments with rivers, but without winds (Riv_1 and Riv_2) are compared with experiments that

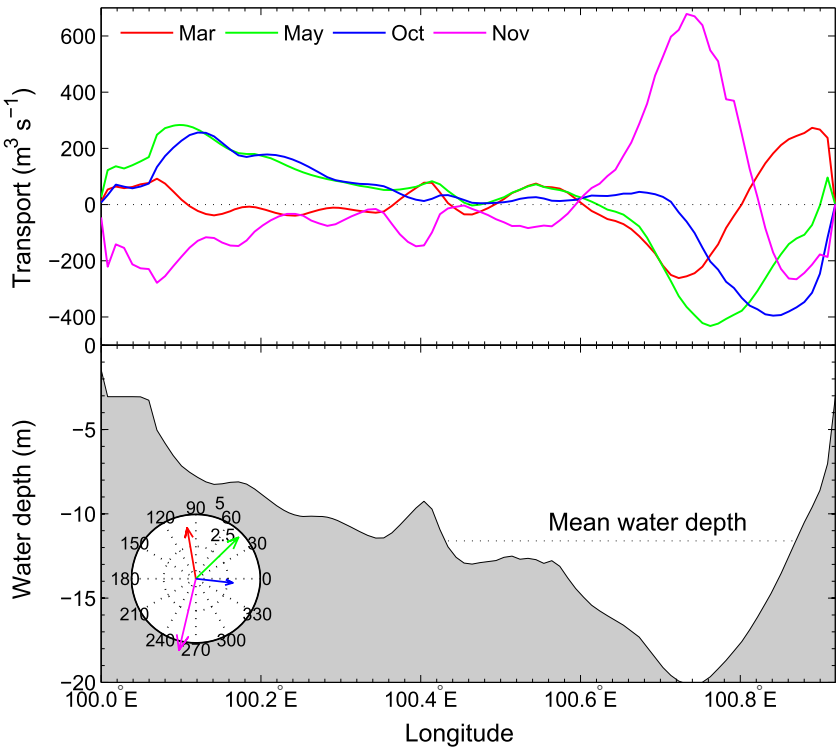

Fig. 7 *Top* North–south transports ($m^3\ s^{-1}$) across latitude 13.35°N (cross-section A-A′) for same months as Figs. 5 and 6: March (*red*), May (*green*), October (*blue*), and November (*magenta*). *Bottom* Topography and monthly mean wind velocity (in $m\ s^{-1}$) for each shown month

include wind forcing (WRiv_1 and WRiv_2). To evaluate the impact of the Coriolis parameter, low-latitude experiments ("exp_1") are compared with mid-latitude experiments ("exp_2"). The simulated monthly mean surface salinity and surface temperature for those experiments are shown in Figs. 8 and 9, respectively. Salinity distribution is shown for September and November to represent months with relatively large amount of water discharge (Fig. 2b), but with different wind directions, while temperature distribution is shown for June (summer monsoon) and November to represent relatively warmer and colder months with different wind directions.

Chao Phraya River, the largest river in the Gulf of Thailand, produces the largest freshwater plume, though the river plume is quickly mixed by the tidal currents even without winds (Fig. 8a, b). The case with a realistic low-latitude Coriolis parameter shows an axisymmetric river plume (Fig. 8a) that is very similar in shape to the observed river plume in Fig. 2a. Symmetric plumes are also found at the other three rivers, but the extent of these plumes is much smaller than that of the Chao Phraya River. The amount of freshwater and intensity of mixing are the key factors that control how far from the river mouth the plume can penetrate. After initial mixing near the river mouth, a tongue of low salinity plume is transported as a buoyancy-driven current along the boundary. The impact of a larger Coriolis parameter is to push the low salinity plume ~30 km farther along the west coast (Fig. 8b in mid latitude relative to Fig. 8a in low latitude). Additional impact of larger Coriolis effect is less axisymmetric plume near the river mouth and the development of a clockwise circulating gyre offshore the river mouth (100.7°E, 42.3°N; Fig. 8b). The classical tendency of the river plume to turn to the right in the northern hemisphere is not seen here, probably due to the strong tidal mixing near the river mouth.

The impact of the wind on the river plume is to push the low salinity plume eastward during the southwest monsoon (Fig. 8c, d) and westward during the northeast monsoon (Fig. 8e, f). The combination of northeast wind and larger Coriolis parameter is especially effective in producing a coastal buoyancy plume that propagate farther along the west coast (almost to the southern edge of the model; Fig. 8f) than any other experiment; the contribution of the wind by itself (without rivers) to this jet can be seen in Fig. 5d.

The impacts of rivers, winds, and Coriolis on surface temperatures (Fig. 9) are quite similar to the impact on salinity. It should be noted first that despite the uniform surface heat fluxes forcing, large spatial variations are seen in the model simulations due to the ocean dynamics; similar spatial variations can sometimes be seen in satellite images (Saramul 2013). These temperature patterns are the result of the fact that the solar radiation will create warmer temperatures near the coast, especially over the shallow regions in the north and west (Fig. 1) where the entire water column (of only a few meters) is warmed up; while in deeper regions, the action of tides cools the surface waters by mixing them with colder water below. The buoyant river plume and winds transport the warm waters along the coast. During the southwest monsoon, the warmest waters are accumulated at the northeastern corner,

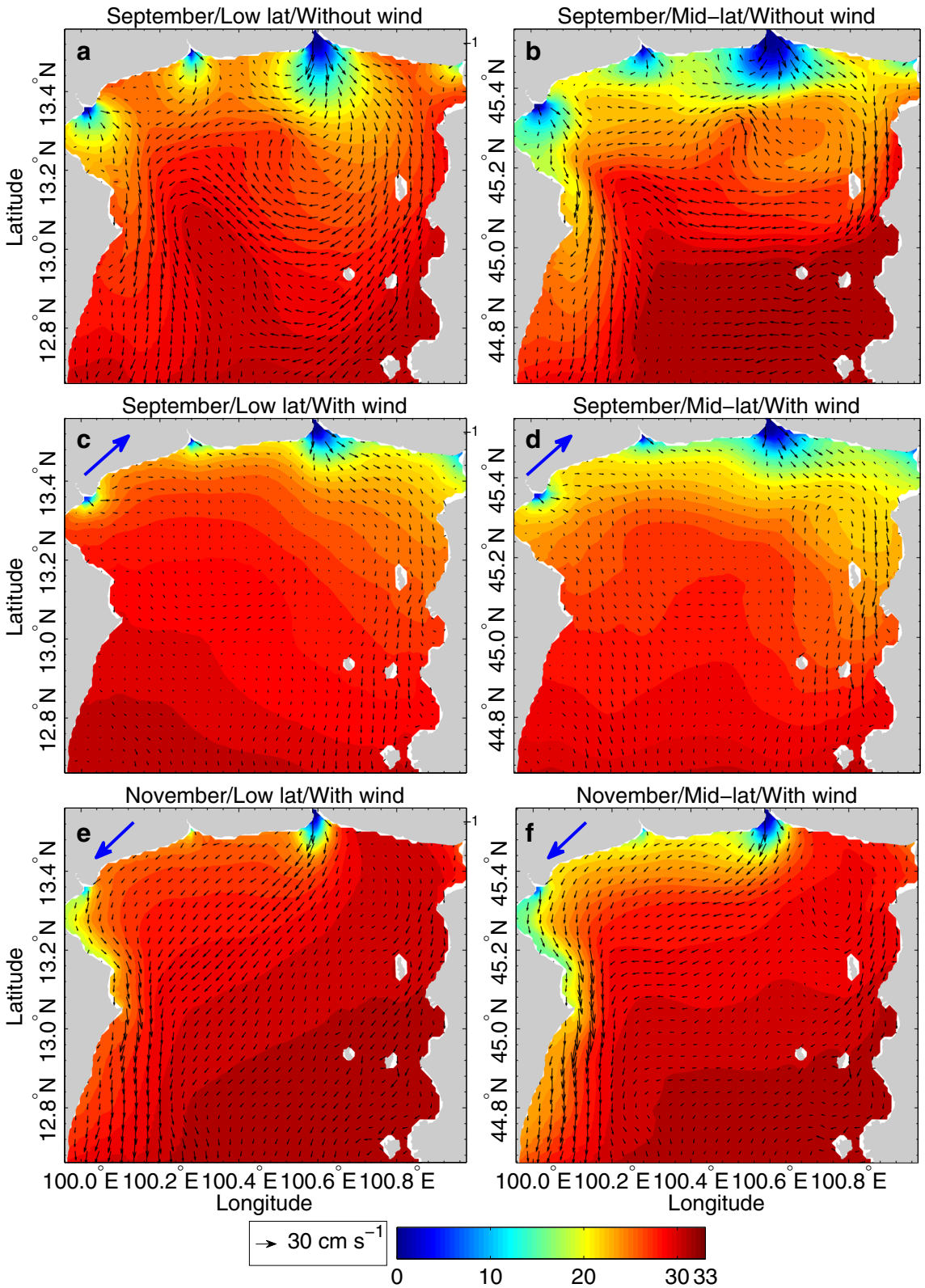

Fig. 8 Model simulations of river plumes showing monthly mean surface current velocity (*black vectors* in cm s^{-1}) and monthly mean surface salinity (in *color*). *Left panels* are simulations with a realistic low latitude location, and *right panels* are simulations at a mid-latitude location. From *top* to *bottom* are simulations without wind (Riv_1 and Riv_2) and with winds (WRiv_1 and WRiv_2) for September (south-westerly monsoon with mean wind speed of 2.7 m s^{-1}) and November (north-easterly monsoon with mean wind speed of 5.7 m s^{-1}). The wind direction in **c**–**f** is shown by the *blue arrows*. The chosen months are those with significant river flow, but different wind direction

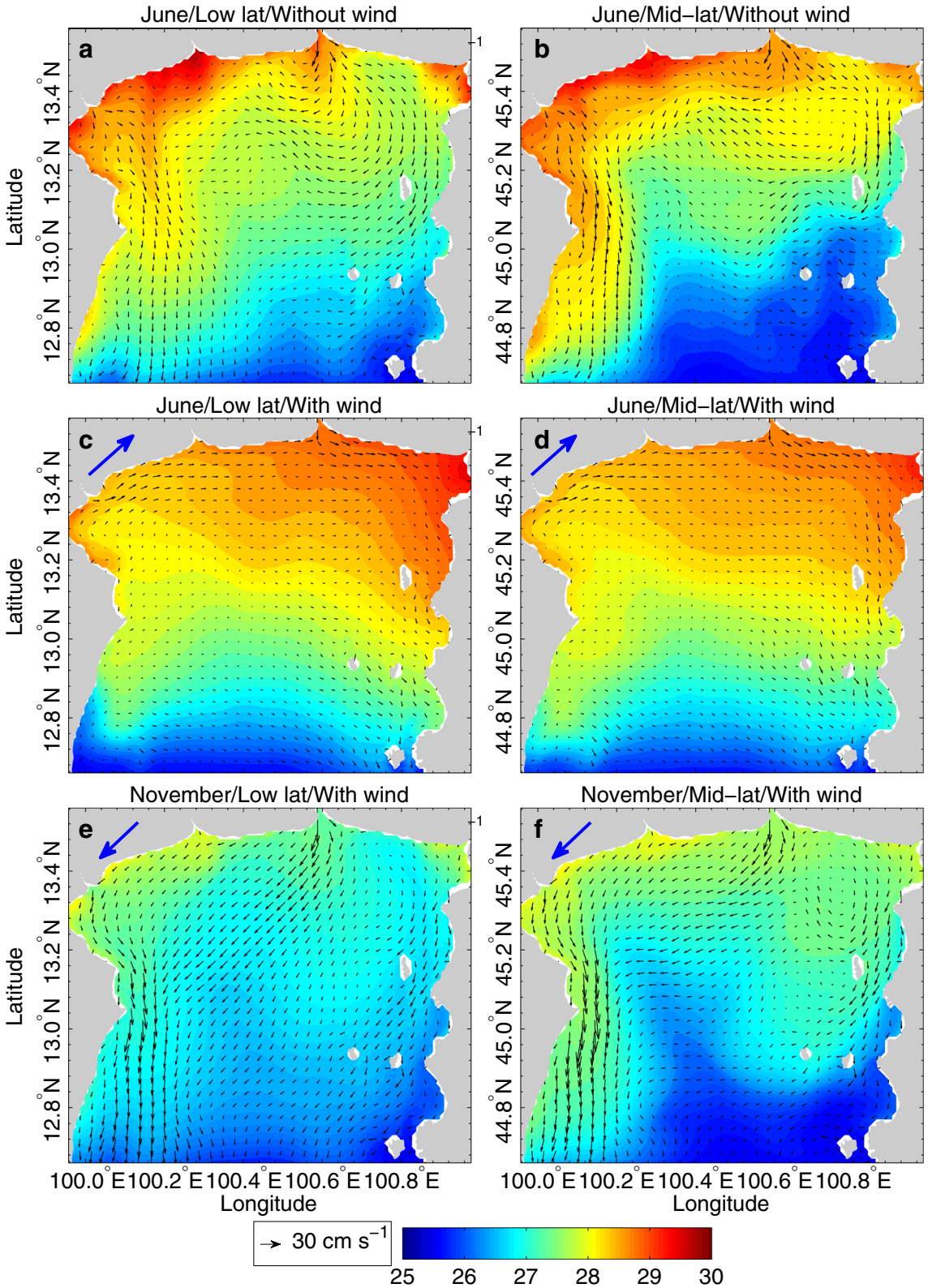

Fig. 9 Same as Fig. 8, but for surface temperatures (color in °C) during June and November 2000. These months were chosen to represent relatively warmer and colder than average months with different wind direction. Wind speeds are 5 and 5.7 m s^{-1} for June and November, respectively

with very little impact from the Coriolis parameter (Fig. 9c, d). During the northeast monsoon, the impact of Coriolis is somewhat larger (Fig. 9e, f) due to a stronger coastal jet along the western boundary. This may be the result of more

pile up of water on the western coast by the Ekman transport and increased geostrophic along-coast flow in mid-latitudes compared with low latitudes.

4 Comparison between the 3D numerical model and an analytical solution

Winant (2004, 2010) described an analytical solution for the wind-driven viscous flow in a closed shallow basin; such a model has been applied for example to the Nansemond River flow, and the results were consistent with observations (Narv'aez and Valle-Levinson 2008). The simple model assumes that the length, L^* of the basin (in the y direction) is larger than the width, W^* (in the x direction), the water depth, H^*, is small and the wind is blowing along the main axis of the basin (y-direction). Because of the narrow width the Coriolis parameter, f, can be neglected. In comparison, the UGOT is shallow and wide, so $L^* \approx W^*$. However, because of its location in low latitudes (i.e., small f), the simple non-rotating solution may still be partly valid for the UGOT. Here it is tested whether or not the simple analytical solution of Winant (2010) can explain the flow derived from the more complex 3D numerical model. The momentum equation in the y direction is assumed to be,

$$\frac{\partial^2 v}{\partial z^2} - \frac{\partial \eta}{\partial y} = 0, \tag{2}$$

where v and η are non-dimensional velocity and surface elevation, respectively. The relation of the dimensionless variables to dimensional variables (marked with stars) are $v = v^* \frac{\rho K_M}{\tau H^*}; \eta = \eta^* \frac{\rho g H^*}{\tau L^*}; x = \frac{x^*}{L^*}; and \;\; z = \frac{z^*}{H^*}$, , where ρ is density of sea water and τ is surface wind stress. After applying boundary conditions at the bottom, $z=-h$, and surface $z=\eta$, the solution is

$$v = \frac{\partial \eta}{\partial y}\left[\frac{z^2 - h^2}{2} - \eta(z+h)\right] + z + h \tag{3}$$

where

$$\frac{\partial \eta}{\partial y} = \frac{3}{2}\frac{\int_{-1}^{1} h^2 dx}{\int_{-1}^{1} h^3 dx} = \frac{3}{2}\frac{h^2}{h^3}. \tag{4}$$

So for a given topography $h(x)$, the velocity $v(x,z)$ driven by wind stress τ can be easily calculated from (3) and (4). The analytical solution was applied to the cross-section along latitude 13.35°N (line A-A′ in Fig. 1) and compared with the 3D numerical model solution during November (Fig. 6h) when the wind was roughly blowing from the north and the sea level gradient is roughly in the north–south direction (Fig. 5d), similar to the $d\eta/dy$ assumed in Eq. 2.

The comparison reveals a similar flow pattern between results obtained from the complex 3D numerical model (Fig. 10a) and the simple analytical solution (Fig. 10b). The flow is northward, against the wind direction, in the deeper channel, and southward, in the direction of the wind, on the shoals on both sides of the channel, as expected from the theory discussed before. Compared with the smoother analytical solution, the 3D model results show larger velocities and more spatial variations associated with gyres and circulation patterns. Given the fact that the 3D solution is a monthly averaged flow of a time-dependent simulation with variable wind and tides, it is somewhat surprising how well it produces a simple steady state analytical solution. The conclusion is that the time-mean flow of this shallow low latitude basin still partly obeys classic non-rotating wind-driven dynamics, though some impact of rotation still exists, as indicated by the Ekman number (Table 2).

5 Interannual variations and ENSO

It is clear from the data in Fig. 3 that in addition to the seasonal variations associated with the monsoonal winds, discussed before, there are also interannual variations, so here results from the multiyear simulations (1997–2000) are analyzed. In those low latitudes, both the net surface heat flux and shortwave radiations have little seasonal or long-term pattern that can explain the variations in surface temperatures (Fig. 3c). Therefore, the main cause of the seasonal and interannual variations in the model temperatures is the combination of the feedback term and cloud cover in Eq. 1. To evaluate how well the model can simulate interannual variations, a comparison is made between the sea surface temperature during 1998, which was an El Niño year, and 2000, which was a La Niña year (Fig. 11).

Sea surface temperatures obtained from the model simulations were spatially averaged in space and daily averaged in time in order to remove tidal and other high-frequency variations. The model results are compared with temperatures obtained from two sources, the reanalysis data (which was used in the feedback term in Eq. 1) and observed temperatures retrieved from AVHRR satellite data for both day time and night time. The latter satellite data were not used in the model and they are only sparsely available during the summer due to increased cloud cover during the wet season. The seasonal pattern of temperatures and the interannual variations are quite well reproduced by the model. However, the model's temperatures are persistently warmer than the reanalysis data; the average error is 0.80 °C±0.29 during 1998 and 0.97 °C±0.29 during 2000. Comparing the model results with the satellite data shows that the mean daily temperature in the model is

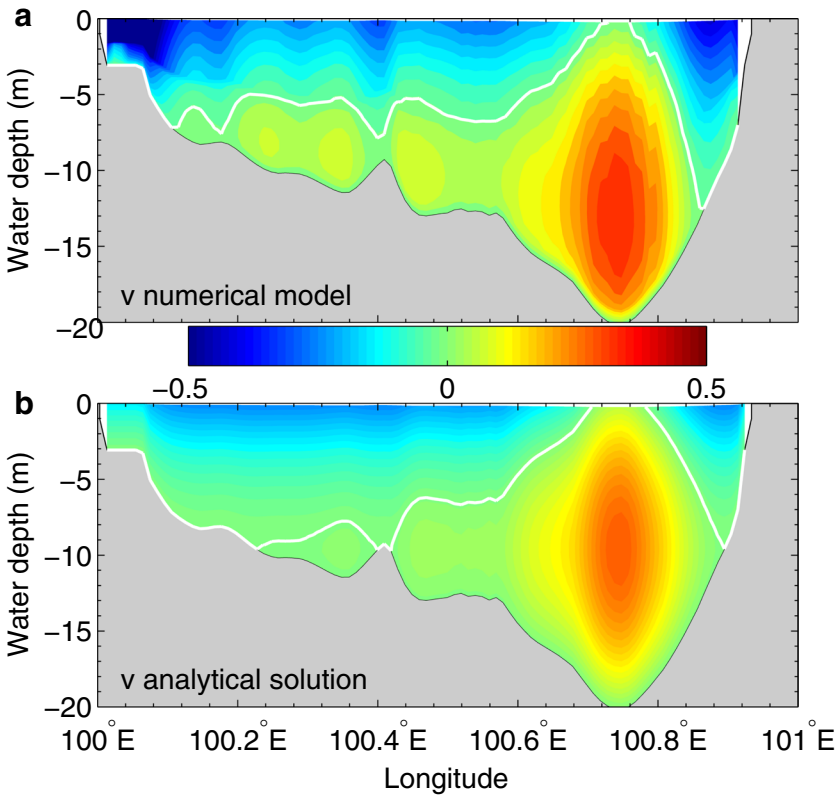

Fig. 10 The *v*-velocity distribution across 13.35°N during the northeast monsoon (November, as *bottom panel* of Fig. 6). **a** From the 3D numerical model simulation and **b** from the analytical 2D model. A *white solid line* represents a zero contour line and the units are non-dimensional. For scaling purposes, the range of the velocity color bar is equivalent to about −6 to 6 cm s^{-1}

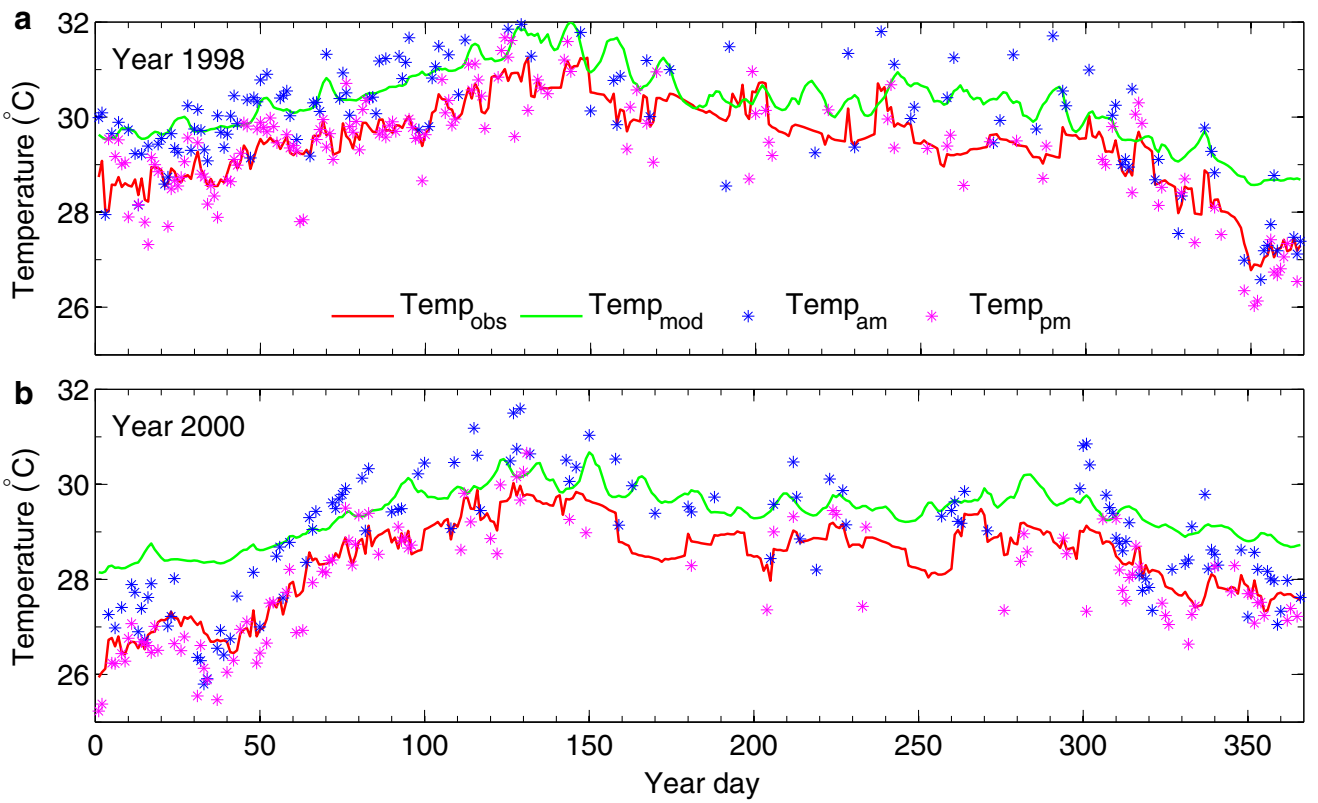

Fig. 11 Area averaged sea surface temperatures (SST) during **a** El Niño year (1998) and **b** La Niña year (2000). SST from model simulations (*green solid line*) is compared with the observed temperature from the reanalysis data (*red solid line*) and with satellite data obtained during the day (*blue stars*) and night (*magenta stars*)

within the daily range, except at the beginning of 2000. In general, the model is doing a better job during the summer monsoon than during the winter season. Note the large daily variations between day and night temperatures, up to 2–3 °C, which cannot be simulated without much higher temporal forcing data. The model also does not take into account potential large-scale changes in the Gulf of Thailand south of the model domain; to account for such changes, a much larger model domain will be needed. In 1998 (an El Niño year), the surface temperature was generally warmer by ~2 °C than that in 2000 (a La Niña year). This difference is attributed to the reduced cloud cover during El Niño events (Fig. 3d; days 300–500 versus days 1,100–1,300) that allows more shortwave radiation to reach the water surface. The El Niño of 1997–1998 was one of the strongest events of the century, which resulted in reduced clouds and dry climate in the western Pacific and the Indonesia region (Chandra et al. 1998), in agreement with our analysis of cloud cover near Thailand. The 1999–2000 La Niña was a more moderate event.

6 Summary and conclusions

A low latitude estuarine-like shallow coastal system, the UGOT, has been modeled to investigate the effects of wind stresses and river discharges on the 3D distribution of salinity, temperature and velocity. While influenced by rivers and tides like other estuarine systems, the UGOT is not a typical estuarine system because of its topography, forcing and location. The UGOT is very shallow and its width equals its length; it is also located in low latitudes where Coriolis effects are small and seasonal monsoonal winds dominate. The UGOT model is based on a 3D primitive equation Princeton Ocean Model. The primary forces are the tides at the southern open boundary, daily surface winds and surface heat fluxes. Monthly mean discharges of four rivers have been included in the simulations; it will be of interest to include interannual variations in river flows in future studies. The simulations show that the circulation in the UGOT is strongly influenced by the seasonal monsoonal winds, which result in a clockwise circulation during the southwest monsoon and counter-clockwise circulations during the northeast monsoon. The southwest and northeast monsoons pile up water in the direction of the winds, but the sea level gradients do not result in geostrophic flows in those low latitudes. Instead, the mean sub-tidal transport resembles a wind-driven non-rotating coastal system such as those described by Csanady (1973) and others. To show this, the time-mean 3D model flow across an east–west section was compared with an analytical solution of a simple wind-driven non-rotating steady state model (Winant 2010). This comparison confirms that the classic pattern of transport in the direction of the wind in shallow regions and transport against the wind in regions deeper than the average depth is still largely valid in the UGOT. However, some rotational influence on the baroclinic flow pattern is not negligible, even in those low latitudes, as seen from analysis of the Ekman number.

Freshwater plumes from rivers play important roles in the UGOT, so sensitivity experiments with the model were conducted to assess the impact of buoyancy-driven versus wind-driven dynamics, and the impact of Coriolis. At low latitudes and without winds, the simulated river plume in the vicinity of the river mouth was found to be axisymmetric (Fig. 8a), a result confirmed by satellite data (Fig. 2a). Farther away from the river mouth a low-salinity plume is spread as a coastal jet along the boundaries. The classic picture of river plumes turning to the right of the outflow when exiting the river mouth (in the northern hemisphere) is not seen here, even when the Coriolis parameter is increased to represent mid-latitudes. The reason is likely the strong tidal mixing which dilutes the river plume when it is still close to the river mouth. However, in the mid-latitude experiments, the plume is less axisymmetric near the river mouth and the diluted low salinity plume spreads farther along the coast than that in low latitudes. The low latitudes also limit the development of small-scale gyres seen offshore the river mouth in mid-latitude simulations. When monsoonal winds are included in the model, the winds dominate the spreading of the plume along the coast in the direction of the wind.

Interannual variations in surface temperatures, as much as ~2 °C difference between one year and another, are due to large-scale atmospheric and climate variations. A comparison between an El Niño year (1998) and a La Niña year (2000) demonstrates the ability of the model to capture these changes. However, unlike higher latitudes where seasonal and interannual variations in surface water temperature are the result of variations in solar radiation and heat fluxes, in the UGOT the most important factor seems to be the change in cloud cover associated with the monsoon (wet and dry seasons) or with the El Niño and La Niña patterns (e.g., the dry climate in the region following the 1997–1998 El Niño; Chandra et al. 1998). Therefore, the cloud cover had to be specifically accounted for in the model fluxes to produce realistic simulations of water temperatures. The model still has some deficiencies, in particular, it does not include the influence from changes in the Gulf of Thailand south of the UGOT; this aspect can be improved by future extension of the model domain to the entire Gulf of Thailand.

In summary, the UGOT model was used here as a test bed to study the dynamics in a unique environment of a shallow low-latitude coastal system with strong influences from river discharges and monsoonal winds. Better understandings of the dynamics and forcing mechanisms in the UGOT can help in the development of future realistic coastal ocean forecast system to address various environmental problems facing this region.

Acknowledgments This study is part of the graduate studies of S. Saramul who received support from ODU's department of Ocean, Earth and Atmospheric Sciences (OEAS), including the Dorothy Brown Smith Scholarship, and from the computational resources of the Center for Coastal Physical Oceanography. Additional support provided by the Thai Government Science and Technology scholarship and from Chulalongkorn University, Thailand. T. Ezer was partly supported by grants from NOAA Climate Programs and the Kenai Peninsula Borough, Alaska.

References

Albretsen J, Røed LP (2010) Decadal long simulations of mesoscale structures in the northern North Sea/Skagerrak using two ocean models. Ocean Dyn 60(4):933–955. doi:10.1007/s10236-010-0296-0

Blumberg, AF, Mellor, GL (1987) A description of a three-dimensional coastal ocean circulation model. In: N. Heaps (ed.) Three-dimensional coastal ocean models. American Geophysical Union, 208pp

Buranapratheprat A, Yanagi T, Matsumura S (2008a) Seasonal variation in water column conditions in the upper Gulf of Thailand. Cont Shelf Res 28:2509–2522

Buranapratheprat A, Yanagi T, Niemann KO, Matsumura S, Sojisuporn P (2008b) Surface chlorophyll-a dynamics in the upper Gulf of Thailand revealed by a coupled hydrodynamics ecosystem model. J Oceanogr 64:639–656

Buranapratheprat A, Niemann KO, Yanagi T, Matsumura S, Sojisuporn P (2009) Seasonal variations in water column conditions in the upper Gulf of Thailand. Burapha Sci J 14(1):99–113

Chandra S, Ziemke JR, Min W, Read WG (1998) Effects of 1997–1998 El Niño on tropospheric ozone and water vapor. Geophys Res Lett 25(20):3867–3870

Chao SY, Shaw PT, Wu SY (1996) El Niño modulation of the South China Sea circulation. Prog Oceanogr 38(1):51–93

Csanady GT (1973) Wind-induced barotropic motions in long lakes. J Phys Oceanogr 3:429–438

Ezer T (2000) On the seasonal mixed layer simulated by a basin–scale ocean model and the Mellor–Yamada turbulence Scheme. J Geophys Res 105(C7):186–195

Ezer T (2013) Sea level rise, spatially uneven and temporally unsteady: Why the U.S. East Coast, the global tide gauge record and the global altimeter data show different trends. Geophys Res Lett 40(20): 5439–5444. doi:10.1002/2013GL057952

Guo X, Valle-Levinson A (2007) Tidal effects on estuarine circulation and outflow plume in the Chesapeake Bay. Cont Shelf Res 27:20–42. doi:10.1016/j.csr.2006.08.009

Guo X, Valle-Levinson A (2008) Wind effects on the lateral structure of density–driven circulation in the Chesapeake Bay. Cont Shelf Res 28:2450–2471. doi:10.1016/j.csr.2008.06.008

Horner-Devine AR (2009) The bulge circulation in the Columbia River plume. Cont Shelf Res 29:234–251. doi:10.1016/j.csr.2007.12.012

Kasai A, Hill AE, Fujiwara T, Simpson JH (2000) Effect of the Earth's rotation on the circulation in regions of freshwater influence. J Geophys Res 105(C7):16,961–16,969

Mellor GL (2004) Users guide for a three-dimensional, primitive equation, numerical ocean model. 35 pp., Program in Atmospheric and Oceanic Sciences. Princeton University, Princeton

Mellor GL, Yamada T (1982) Development of a turbulence closure model for geophysical fluid problems. Rev Geophys 20(4):851–875

Narv'aez DA, Valle-Levinson A (2008) Transverse structure of wind–induced flow at the entrance to an estuary: Nansemond River. J Geophys Res 113(C09004), DOI 10.1029/2008JC004770

Nicholls RJ (2011) Planning for the impact of sea level rise. Oceanography 24(2):142–155

Oey LY (1996) Simulation of mesoscale variability in the Gulf of Mexico: Sensitivity studies, comparison with observations, and trapped wave propagation. J Phys Oceanogr 26(2):145–175

Sanay R, Valle-levinson A (2005) Wind–induced circulation in semienclosed homogeneous, rotating basins. J Phys Oceanogr 35: 2520–2531

Saramul S (2013) Observations and modeling forcing mechanisms for the coastal dynamics of the Upper Gulf of Thailand. Ph.D. Dissertation, Old Dominion University, 154 pp

Saramul S, Ezer T (2010) Tidal-driven dynamics and mixing processes in a coastal ocean model with wetting and drying. Ocean Dyn 60(2): 461–478. doi:10.1007/s10236-009-0250-1

Valle-Levinson A, Reyes C, Sanay R (2003) Effects of bathymetry, friction, and rotation on estuary–ocean exchange. J Phys Oceanogr 33:2375–2393

Winant CD (2004) Three-dimensional wind-driven flow in an elongated, rotating basin. J Phys Oceanogr 34:462–476

Winant CD (2010) Wind and tidally driven flows in a semienclosed basin. In: Valle-Levinson A (ed) Contemporary Issues in Estuarine Physics, 1st edn. Cambridge University Press, New York, pp 125–144

Wong KC (1994) On the nature of transverse variability in a coastal plain estuary. J Geophys Res 99(C7):14,209–14,222

Yu L, Jin X, Weller RA (2008) Multidecade global flux datasets from the Objectively Analyzed Air–sea Fluxes (OAFlux) Project: Latent and sensible heat fluxes, ocean evaporation, and related surface meteorological variables. Tech. Rep. OA-2008-01, Woods Hole Oceanographic Institution, Woods Hole, Mass

Zheng L, Weisberg RH (2004) Tide, buoyancy, and wind–driven circulation of the Charlotte Harbor estuary: A model study. J Geophys Res 109(C06011), DOI 10.1029/2003JC001996